THE JOURNAL OF PHYSICAL CHEMISTRY C
A JOURNAL OF THE AMERICAN CHEMICAL SOCIETY

pubs.acs.org/JPCC

Article

ZnO Nanostructures Application in Electrochemistry: Influence of Morphology

Agne Sulciute, Keita Nishimura, Evgeniia Gilshtein, Federico Cesano, Guido Viscardi, Albert G. Nasibulin, Yutaka Ohno, and Simas Rackauskas*

Cite This: J. Phys. Chem. C 2021, 125, 1472−1482

Read Online

ACCESS | Metrics & More | Article Recommendations

ABSTRACT: The aim of this work was to investigate the influence of morphology on its electrochemical properties by comparing ZnO nanostructures in the forms of tetrapods of different sizes, nanorods, and nanoparticles. ZnO tetrapods were prepared by the combustion method and separated into two fractions by size, ruling out the influence of synthesis conditions. Structural and morphological properties of different ZnO nanostructure morphologies were identified by using various characterization techniques: scanning and transmission electron microscopies (SEM and TEM), X-ray powder diffraction (XRD), nitrogen adsorption/desorption measurements at 77 K, and UV−vis spectroscopy (UV−vis). Analysis of electrochemical properties showed the highest active surface area of 0.095 cm^2 and the lowest peak separation value of 61.7 mV for large ZnO tetrapods, which are close to the theoretical values. The correlation between the pore size in different ZnO nanostructures because of packing and their electrochemical properties is established. We expect that the detailed analysis of ZnO nanostructures conducted in this study will be advantageous for future electrochemical and biosensing applications of these materials.

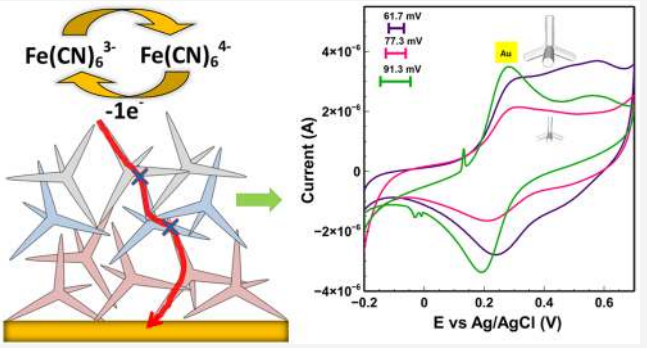

1. INTRODUCTION

ZnO is an n-type semiconductor material with wide bandgap (3.37 eV) and high exciton binding energy (60 meV). The outstanding popularity of ZnO and their nanostructures application are constantly increasing. The ZnO multifunctionality is interesting for various applications, such as catalysts,[1] photovoltaics,[2,3] sensors,[4−9] mixed oxide varistors,[10] rubber,[11] and concrete additives,[12,13] serving to large-scale industry needs. ZnO nanostructures can be manufactured by using miscellaneous synthesis methods that, according to the processes used, can be divided into chemical synthesis methods—hydrothermal synthesis,[14−16] combustion,[17−20] electrochemical deposition,[21] chemical vapor deposition,[22−24] spray pyrolysis,[25] and so on—and physical methods—arc discharge method,[26,27] radio-frequency magnetron sputtering,[11,28] molecular beam epitaxy,[29] pulsed laser deposition,[30] and so on.

Depending on synthesis conditions, the structure and morphology can be significantly modified wherefore physical and chemical properties alter. ZnO has three main fast growth directions ([0001], [$2\bar{1}\bar{1}0$], and [$01\bar{1}0$]), and by changing synthesis conditions, we can obtain a variety of ZnO nanostructures. This material is synthesized with versatile controlled shapes and sizes, such as nanoparticles,[2,4,11−13,31−33] nanorods,[14,34−36] nanotubes,[3] nanobelts,[10] tetrapods,[18,37−40] rings,[41] bowls,[41] hemispheres,[41] disks,[41] flowers,[42] and so on.

Many works are devoted to the physical and electrochemical property dependence on ZnO structure. The control of the size and the shape of ZnO nanostructures is essential for many advanced applications.[1,3,10,11,43] Therefore, there are many studies done to investigate the size and shape influence on physical properties (photoluminescence, transmittance, absorbance, etc.[14,44]) and electrochemical properties (photocatalytic activity, peak separation, active surface, potential window measurements, etc.[1−3,27,43,45−48]). Until now the dependence of the ZnO nanostructure forms on the electrochemical performance of this material is not evident.

Morphological and structural properties of the material strongly affect its properties and, therefore, define electrochemical applications. The structure of the electrode surface contributes to the cyclic voltammetry characteristics and is

Received: September 16, 2020
Revised: December 22, 2020
Published: January 6, 2021

https://dx.doi.org/10.1021/acs.jpcc.0c08459
J. Phys. Chem. C 2021, 125, 1472−1482

essential for several important parameters such as the active electrode area calculated by the Randles−Sevcik equation and peak separation to determine the number of electrons transferred. Therefore, a cyclic voltammetry study using potassium ferricyanide, as an indicator, is a convenient tool for surface characterization of electrodes, where the charge transfer at the interface between electrolyte and electrode must occur either by a barrier or through defects. Because ΔE_p is a function of electron transfer rate, hence the lower the ΔE_p, the greater the electron transfer rate, thus minimizing the background current.[49] Furthermore, ΔE_p values vary due to the electrode active surface, defects, material, varying potential interval, sweep rate, electrolyte and its concentration, and pH value.[50−52]

Therefore, the aim of this work is to investigate the influence of ZnO nanostructure morphology (size, shape, and porosity) on its electrochemical properties. Thus, we used different morphologies of ZnO nanostructures for comparison: (i) ZnO tetrapods (ZnO-Ts) which we synthesized by the combustion method[18] and separated into two fractions by size; (ii) commercially available ZnO nanorods and nanoparticles. ZnO-Ts of different sizes were made under the same conditions (temperature, synthesis time, etc.) and afterward were separated by centrifugation into two fractions by size, in such a way ruling out the influence of synthesis conditions on their properties. To estimate the structure and morphology influence on electrochemical properties, SEM, TEM, BET, XRD analysis, and UV−vis spectroscopy were used; electrochemical properties were measured by using cyclic voltammetry, employing Au electrodes with a thin film of ZnO nanomaterial. Compared to other ZnO nanostructures, large ZnO-Ts demonstrated the lowest peak separation and the highest active surface values, which can be attributed to their pore size and shape.

2. MATERIALS AND METHODS

2.1. ZnO Nanostructure Preparation. ZnO-Ts were synthesized by the combustion method as described in previous work.[18] Briefly, micrometer-sized Zn particles were introduced from the top ending of the quartz tube into a vertical furnace under an ambient air atmosphere. During the combustion process occurring at 1173 K, ZnO-Ts were formed, and the obtained powder was collected from the bottom ending of the quartz tube on a filter. As-obtained ZnO-Ts were dispersed in absolute ethanol and separated by centrifugation using two rotation speeds (1000 and 3000 rpm) into two different fractions of the supernatant of the liquid, and these fractions were used in this work. The size of the particles that precipitate due to centrifugal force is proportional to the particle size; therefore, larger diameter ZnO-Ts (LT, Table 1) were obtained in the supernatant solutions at 1000 rpm compared to smaller ZnO-Ts after 3000 rpm (ST).

ZnO nanoparticles from Sigma-Aldrich (product no. 544906), particle size <100 nm, are produced by a vapor method using electric arcs to vaporize precursor materials, which are then carefully condensed to produce nanoparticles. In this paper nanoparticles are labeled as NP (Table 1).

ZnO nanoparticles from Sigma-Aldrich (product no. 544906), particle size <100 nm, are produced by a vapor method using electric arcs to vaporize precursor materials, which are then carefully condensed to produce nanoparticles. In this paper nanoparticles are labeled as NP (Table 1).

Table 1. ZnO Nanostructures Used in This Work

sample notation	ZnO morphology	diameter (nm)	length (nm)	origin
LT	large tetrapods	10−20 (leg)	125−150 (leg)	centrifuged at 1000 rpm
ST	small tetrapods	5−10 (leg)	50−60 (leg)	centrifuged at 3000 rpm
NP	nanoparticles	40	80	commercial product
NR	nanorods	60	160	commercial product

Commercially available ZnO (Kadox-25, New Jersey Zinc Co.) obtained by combustion of zinc metal, exhibiting wurtzite crystal nanocrystals with the prevalence of hexagonal facets,[53] was used for comparison. ZnO Kadox nanocrystals show a moderate aspect ratio, and a predominant nanorod-like structure can be assumed. All ZnO nanostructures were not modified, and commercial ZnO nanostructures were used as received.

The working electrode was prepared on a glass substrate by sputtering of 100 nm thick, 10 mm long, and 5 mm wide gold strip through the mask. A layer of ZnO nanostructures was deposited on a glass substrate heated to 353 K by airbrush spraying of 1 mg/mL solution of ZnO nanostructures in ethanol after mild sonication. Silver paint was used for the low resistance contact with potentiostat clips on the part, which was not immersed into the liquid.

Resistivity measurements of ZnO nanostructures were made by using ZnO nanostructure solutions in ethanol after mild sonication and deposited by airbrush spraying between two electrodes with a gap of 20 μm on a glass substrate heated to 353 K; the layer thickness was kept at 15 μm for all ZnO nanomaterials. Measurements were performed at room temperature (298 K) with ambient air (30% RH); the resistivity was calculated from the $I-V$ curve linear region −5 to −10 V as $R = dV/dI$.[54]

2.2. Electrochemical Stability Window (Cyclic Voltammetry and Potential Window Measurement). The electrochemical measurements were performed by a computer-controlled potentiostat (Metrohm, Autolab). A standard three-electrode cell (volume 100 mL) was used. The potential window measurement was made in 20 mL of 0.1 M KCl electrolyte solution. Measurement of ΔE_p was made with 100 μM $K_4[Fe(CN)_6]$ dissolved in 0.1 M KCl. During the electrochemical measurements an Ag/AgCl reference electrode (RE) of 2 mm diameter (World Precision Instruments, DRIRFE-2) and a Pt counter electrode (CE) of 0.5 mm diameter (Bio-Logic Science Instruments, A-002222) were used. The working electrode was a glass electrode covered with various ZnO nanostructures on a gold strip. For all types of ZnO nanostructures the coating thickness was maintained at 5 μm. The simplified electrochemical measurements setup and SEM images of various ZnO nanostructures used in this study are shown in Figure 1.

The potential window was evaluated by using cyclic voltammetry measurements, which were made by using 0.1 M KCl solution as electrolyte. Potassium hexacyanoferrate(II), $K_4[Fe(CN)_6]$, in the amount of 100 μM (99.5% purity) was used for electron transfer measurements. Only freshly prepared solutions were used for the measurement and were not deaerated during the experimental runs.

https://dx.doi.org/10.1021/acs.jpcc.0c08459
J. Phys. Chem. C 2021, 125, 1472−1482

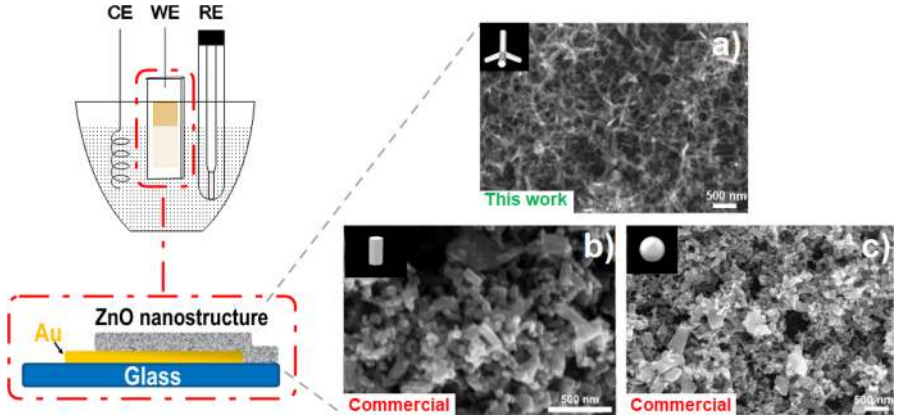

Figure 1. Schematics of the experimental setup for electrochemical measurements. The electrochemical quartz cell filled with 100 μM $K_4[Fe(CN)_6]$ dissolved in 0.1 M KCl for ΔE_p and active surface measurements. RE: Ag/AgCl reference electrode; WE: working electrode; CE: platinum wire as a counter electrode. SEM images of ZnO nanostructure: (a) ZnO tetrapod mix before separation, (b) Kadox-25 nanorods (NR), and (c) ZnO nanoparticles (NP).

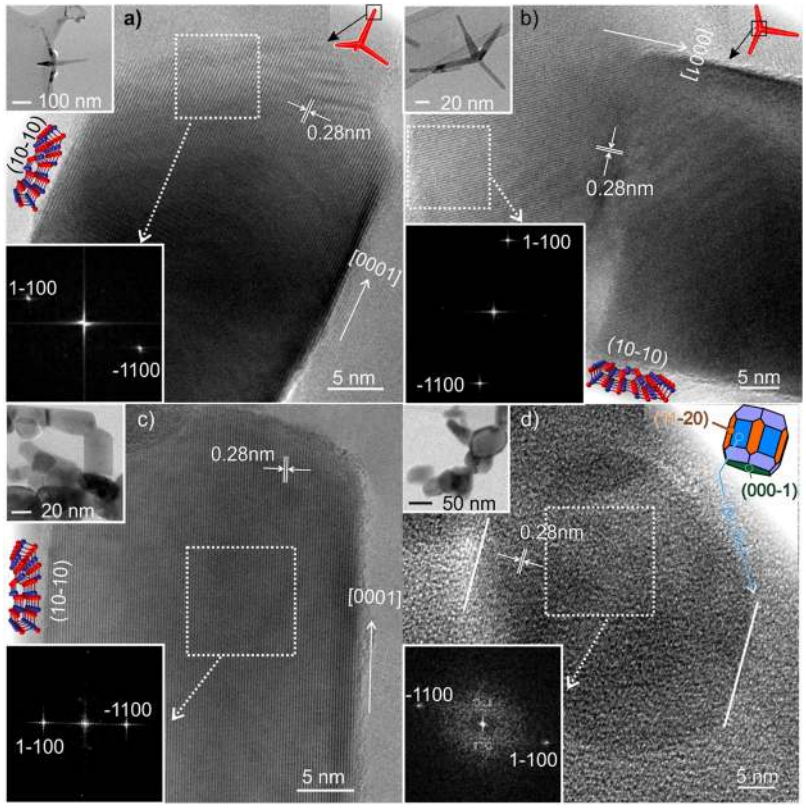

Figure 2. TEM and HRTEM of ZnO tetrapods after centrifugation at (a) 1000 rpm (LTs) and (b) 3000 rpm (STs). (c) ZnO nanorods and (d) ZnO nanoparticles. Representation of the $(10\bar{1}0)$ nonpolar surfaces is shown in (a–c), while the simulated surface of the ZnO nanoparticles is illustrated in (d). In the top-right insets, representations of the HRTEM selected regions of tetrapods are depicted. In the bottom-left insets, fast-Fourier transform (FFT) images of the selected regions in (a–d) are illustrated.

2.3. Structural Characterization. A PANalytical X'Pert PRO XRD diffractometer was used for the X-ray powder diffraction (XRD) measurements. Technical specification: Ni filtered Cu radiation in a standard Bragg–Brentano geometry. The International Centre for Diffraction Data (ICDD) database was used to compare XRD patters and to identify the phase. The Debye–Scherrer equation was used to calculate crystallite sizes; the constant k_1 value of 0.94 was used in this work.[55]

A Zeiss Evo50 SEM instrument connected with an Oxford energy dispersive X-ray detector was used. In addition, a JEOL 3010-UHR TEM instrument with 300 kV operating voltage was used to investigate the crystalline structure of the samples. Technical specifications: 300 kV, 2K × 2K pixels Gatan US1000 CCD camera.

To determine the Brunauer–Emmett–Teller (BET) surface area and the porosity properties, characterization of the samples' surface area and N_2 adsorption–desorption measure-

https://dx.doi.org/10.1021/acs.jpcc.0c08459
J. Phys. Chem. C 2021, 125, 1472–1482

ments were performed at 77 K on a Micromeritics ASAP 2020 instrument.

A double-beam UV−vis spectrophotometer (Varian Cary UV 300 Bio) was exploited for optical absorbance measurements in the wavelength range 190−800 nm. All samples were dispersed in absolute ethanol, and spectra were estimated in the transmission mode.

Veusz, Edraw Max 9.2, and Adobe Photoshop CC 2019 image acquisition tools and image processing software packages were used. Shape software was used for the external morphology (faces) representation of crystals.

3. RESULTS AND DISCUSSION

3.1. Morphology and Structure. We synthesized ZnO tetrapods exploiting the combustion method,[17,18] which has several advantages, such as low cost as well as continuous and high yield synthesis.[18,19] ZnO-Ts subsequently were separated by size into two fractions by using a centrifuge: large ZnO tetrapods were collected at 1000 rpm and small tetrapods at 3000 rpm. Therefore, since the ZnO tetrapod structure was not affected by synthesis conditions, it gives the opportunity to investigate how the morphology (i.e., dimensions) influences the electrochemical properties.

To compare various morphologies, commercially available ZnO nanostructures were used. High aspect ratio commercial ZnO nanostructures, i.e., nanorods, were manufactured by using the chemical vapor deposition method. Other commercial ZnO nanomaterials with low aspect ratio, i.e., nanoparticles, were synthesized by using the physical arc discharge method. Moreover, ZnO NRs were synthesized by the chemical route (chemical vapor deposition), whereas ZnO NPs were synthesized by the physical route, condensing nanoparticles after arc discharge. This gives a possibility to evaluate electrochemical properties of two distinct ZnO nanostructure synthesis methods.

From SEM images of the electrode containing the different ZnO nanostructures illustrated in Figures 1, a particular orientation of the tetrapod structures with respect to the other nanostructures (nanorods and nanoparticles) can be observed. This characteristic will be discussed later when morphology and structure as obtained by TEM images will be shown.

Figure 2a−d shows TEM and HRTEM images of STs, LTs, NRs, and NPs. ZnO-Ts prepared by the earlier developed combustion method have a typical tetrapod structure consisting of four connected nanorods (legs) as imaged in the low-resolution TEM images (top-left insets of Figure 2a,b). ZnO tetrapods collected after 3000 rpm (STs) have smaller leg diameters (5 nm) and shorter length (50 nm) compared to those collected after 1000 rpm (LTs), which exhibit mean diameters and leg lengths of 20 and 150 nm, respectively. The atop leg region of a ST is HRTEM imaged in Figure 2a, where well-defined interference fringes corresponding to ZnO $(10\bar{1}0)$ planes, as obtained from the fast-Fourier transform (FFT) images (bottom-left inset of Figure 2a), show two bright spots which are associated with 0.28 Å regularly spaced planes. The bottom region of a leg (ST) is HRTEM imaged in Figure 2b. Well-defined interference fringes corresponding to ZnO $(10\bar{1}0)$ planes, as obtained from the FFT images (bottom-left inset of Figure 2b), show two bright spots which are associated with 0.28 Å regularly spaced planes. HRTEM shows the highly crystalline structure of ZnO-Ts; the most exposed surfaces are laterally exposed prismatic (nonpolar) facets of ZnO-T legs.

ZnO NRs calcined at 400 °C display a hexagonal prismatic habit (top-left inset of Figure 2c) with a typical preferential growth direction. A more precise investigation reveals that the ZnO crystals are elongated along the prismatic $(10\bar{1}0)$ direction and are highly crystalline, as testified by the 0.28 Å spaced well-defined interference fringes, whose corresponding SAED pattern is imaged in the bottom-left inset of Figure 2c. Furthermore, such ZnO nanocrystals have apparently rounded terminations made of small facets together with defects (terraces and steps).[56]

It is not surprising that ZnO-Ts and NRs expose the [0001] preferential growth direction due to the fact that their synthesis involves high-temperature treatments, under which $\{10\bar{1}0\}$ and $\{11\bar{2}0\}$ prismatic facets are more stable,[56] while {0001} facets, formed of only one type of ion (polar surfaces), may reconstruct with the formation of microsteps.[57] In the case of the ZnO NPs the situation is completely different (Figure 2d). Nanoparticles are larger (50−80 nm), exposing a more complex habit, which is composed of a variety of surfaces due to their shapes (top-left inset of Figure 2d); as also shown in the ZnO constructed crystal (Figure 2c), interference fringes with 0.28 Å space correspond to $(10\bar{1}0)$ planes. We can conclude that because of their morphology, ZnO NPs exhibit a larger amount of polar terminations compared to ZnO elongated structures.

It is important to emphasize that tetrapods by their nature are made of legs branching radially from the joint region, in a way that if a tetrapod is on a flat surface, one leg is always arranged vertically, while the others are oriented downward. This characteristic can be a determining factor for electron transport lowering the number of needed junctions in percolation path of tetrapod based layer compared to a more complex path of other geometries due to jump from one nanoparticle to another. A HRTEM image of a connection region of tetrapods is shown in Figure 3.

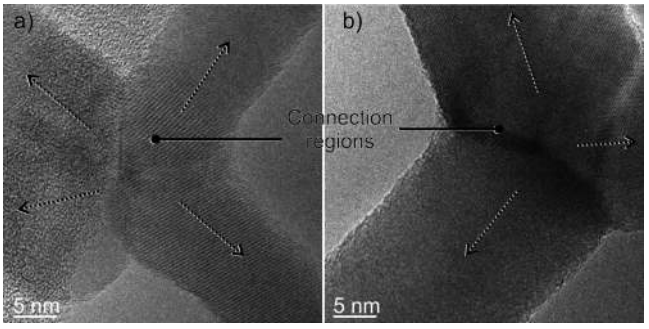

Figure 3. HRTEM images illustrating four leg joint regions in (a) STs and (b) LTs. Leg preferential directions are also illustrated.

UV−vis spectroscopy was used to study the optical properties of the ZnO nanostructures. UV−vis spectra of various ZnO nanostructures dispersed in absolute ethanol are shown in Figure 4a. Because of the direct electron transitions from the valence band to the conduction band, a sharp absorption in the 350−600 nm interval is seen. The spectra reveal a characteristic absorption peak of ZnO at the wavelength of ∼370 nm, which can be assigned to the intrinsic band gap absorption of ZnO due to the electron transitions from the valence band to the conduction band ($O_{2p} \rightarrow Zn_{3d}$).[58,59] Comprehensively, moving from the pink curve (ST) (Figure 4a, inset) to the dark violet curve (LT), and then up to

https://dx.doi.org/10.1021/acs.jpcc.0c08459
J. Phys. Chem. C 2021, 125, 1472−1482

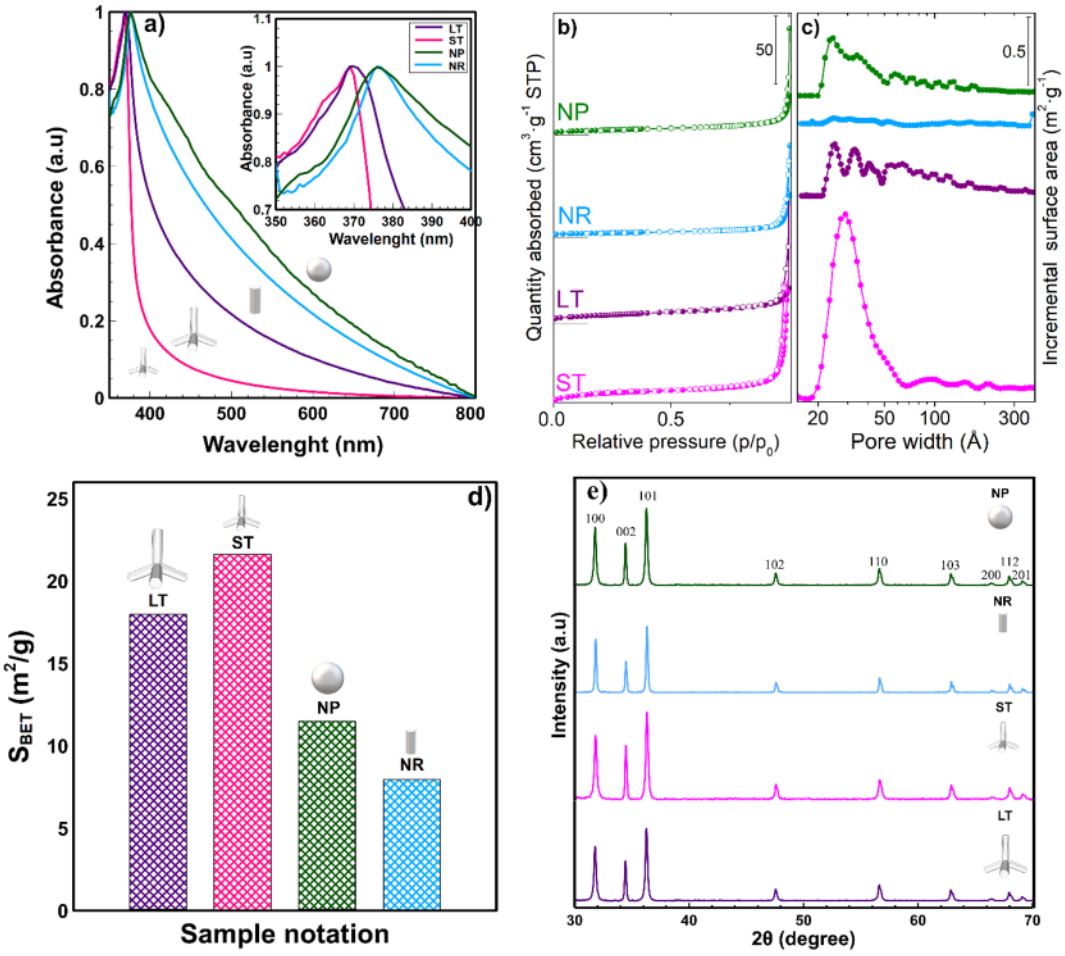

Figure 4. ZnO nanostructure characterization: (a) UV−vis spectra of various ZnO nanostructures dispersed in absolute ethanol. Inset shows a close-up of the absorption peak. (b) N_2 adsorption/desorption curves. (c) Pore size distributions in the 10−40 Å range. (d) Surface area (BET), calculated from N_2 adsorption/desorption measurements. (e) XRD pattern.

the light blue (NR) and dark green curves (NP), a shift to the higher wavelength is observed. The peak shift for smaller ZnO nanostructures can be associated with the quantum size effects. It is worthy to note that NRs and NPs behave as 3D systems because of their roughly remarkable sizes, while TPs approach properties of low-dimensional systems (i.e., leg diameter). Decreasing the ZnO size leads to smaller excitation frequencies. A blue-shift is observed in the extinction behavior, and the absorption edge is positioned at smaller wavelengths.[60] It can be seen that with the increase of the particle size and shape, the slope of the shoulders becomes steeper (Figure 4b, LT and ST curves). This can be associated with the increase of the visible part scattering effects for larger ZnO nanostructures.[17]

N_2-adsorption/desorption isotherms at 77 K and the associated pore size distributions (PSDs), determined by applying the DFT (density functional theory) method, of the ZnO nanostructures after the electrode preparation are shown in Figure 4. All isotherms are of type IV with hysteresis loops, indicating the mesoporous character. The contribution of small micropores is negligible. This observation is confirmed by PSDs reported in Figure 4b. In more detail, a very broad distribution of pores in the 20−400 Å range is shown for all samples, with larger contribution of the smaller mesopores (20−60 Å). Interestingly, this prominent distribution is remarkably intense for the ZnO ST and roughly negligible for the ZnO NR sample. The weak hysteresis loop observed for the adsorption/desorption isotherms (Figure 4b) and the wide distributions of the pore sizes (Figure 4c) can be explained with a porosity coming from the aggregation state of the ZnO tetrapods, nanorods, or nanoparticles in the electrode.[61] In fact, while for short tetrapods (ST), nanorods (NR), and nanoparticles (NP) the empty spaces could be more efficiently filled, the packing of the long tetrapods (LT) is prevented by their long legs.

The BET surface area values and pore sizes of the ZnO nanostructures, calculated from the N_2-adsorption isotherms, are summarized in Figure 4d. Tetrapod-shaped ZnO nanostructures had the highest surface area compared to ZnO NRs and NPs. Also it is known that BET analysis evaluates only the open pores. Because of this, the tetrapods may accumulate and form agglomerates with the closed type pores (intercluster pores).[62] We can assume that all samples exhibited a broader and extended mesoporosity. Because of mesoporosity properties developing a high specific surface area, molecular species can be adsorbed; therefore, finally pore filling occurred through capillary condensation governed by various factors largely of kinetic origin.[62]

It can be concluded that even though the surface area of all ZnO nanostructure is in the range 8−22 m^2/g (Figure 4b,c), the best results are obtained with ZnO LTs and STs, probably due to higher porosity they created in the film assembling.

https://dx.doi.org/10.1021/acs.jpcc.0c08459
J. Phys. Chem. C 2021, 125, 1472−1482

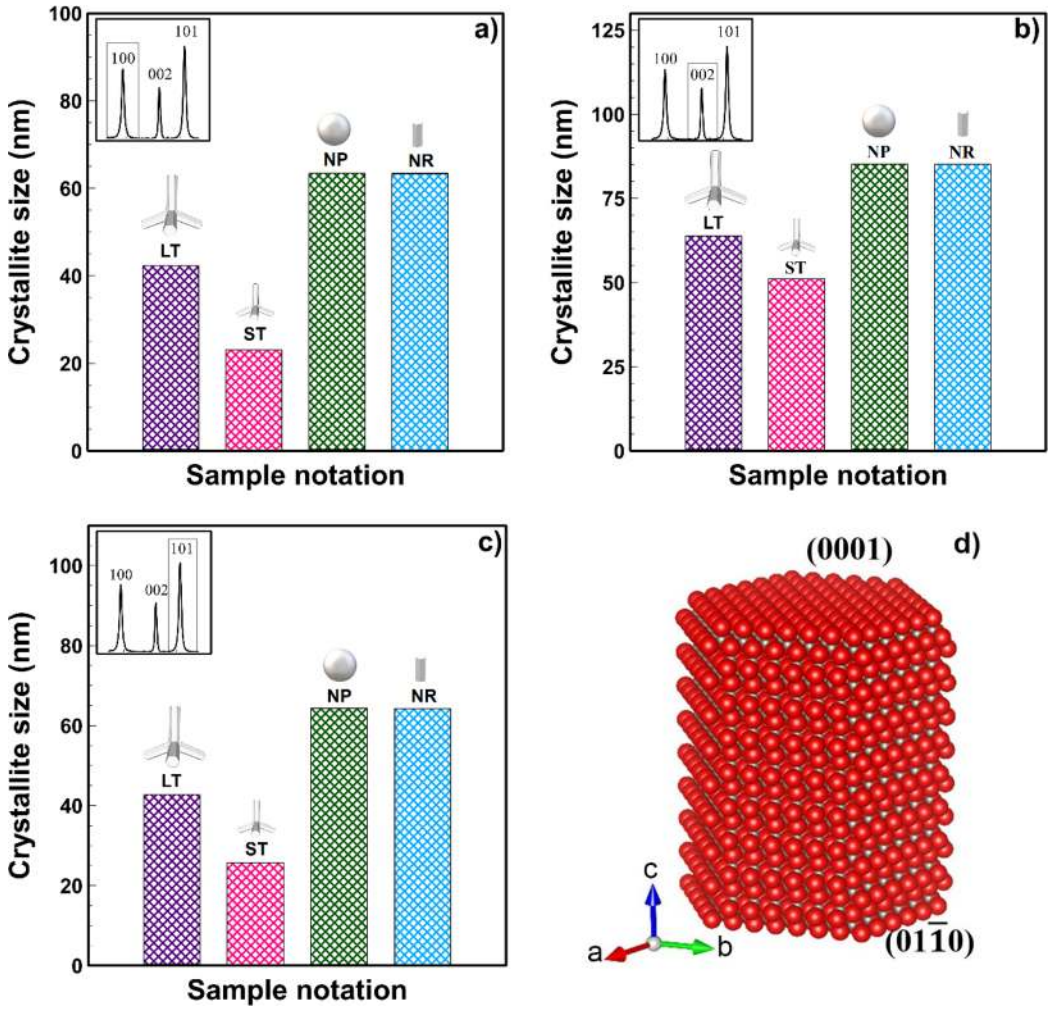

Figure 5. Sizes of ZnO nanostructure crystallites obtained from the Debye−Scherrer formula for planes (a) (100), (b) (002), and (c) (101). (d) ZnO NR crystal structure; Zn and O are marked by silver and red spheres, respectively.

The crystal structure and orientation of the as-grown ZnO particles were investigated with XRD analysis. The crystallite size for ZnO was calculated from X-ray diffraction profiles of stronger relative intensity by measuring the full width at half-maximum (FWHM) and applying the Debye−Scherrer equation.

The ZnO nanostructures were scanned over the range 2θ = 30°−70°. ZnO tetrapod, nanorod, and nanoparticle patterns are illustrated in Figure 4e. No impurity peaks are observed in the patterns. Such strong and sharp peaks at $2\theta \sim$ 31.8°, 34.5°, 36.3°, 47.6°, 56.6°, 62.9°, 66.4°, 67.9°, and 69.1° in the XRD patterns correspond to (100), (002), (101), (102), (110), (103), (200), (112), and (201) planes of hexagonal wurtzite ZnO structure, respectively (JCPDS card #36-1451).

The results obtained from the Debye−Scherrer equation show a significant increase in FWHM values from 0.136 for nanoparticles to 0.37 for small ZnO-Ts. The FWHM is sensitive to the variation in microstructure; therefore, it affects the size of the crystals. The increasing FWHM values can be due to the decrease of ZnO crystal sizes: from ∼63 to 23 nm and from ∼85 to 61 nm. The obtained results for different faces are reported in Figure 5. An increase in stacking faults and structural disorder widens the XRD peaks.[63]

3.2. Electrochemical Properties. It is known that electrochemical deposition parameters (potential, temperature, time, surface coverage, and compactness) affect ΔE_p values. For example, Zawawi et al.[52] determined that the anodic peak current increased and the peak potential shifted to a more positive potential with the decrease in temperature, and the ZnO electrode prepared at 333 K was quasi-reversible with a peak separation of 0.42 V.[52] It was also determined that the ZnO-modified ITO (indium tin oxide covered glass) prepared at −0.9 V deposition potential showed the smallest ΔE_p value compared to electrode prepared at −1.0 and −1.1 V. However, to the best of our knowledge, there is no systematic analysis of the ZnO nanomaterial shape and morphology influence on the electrochemical peak separation value (ΔE_p).

Therefore, we compared the influence of various ZnO nanostructure morphologies on electrochemical properties, such as potential window, peak-to-peak separation, and calculated active surface.

3.2.1. Electrochemical Reactions of ZnO Nanostructures under Different Potentials. The potential window, showing the electrochemical stability of solvents and electrolytes, is an important measure for determining the oxidation and reduction potential.[64] The electrochemical characteristics of potential window for the ZnO nanostructures were estimated from the cyclic voltammograms in a 0.1 M KCl solution (Figure 6). The scan range of −0.2 to 0.7 V (vs Ag/AgCl) and the scan rate of 25 mV s^{-1} were used. Even though the

https://dx.doi.org/10.1021/acs.jpcc.0c08459
J. Phys. Chem. C 2021, 125, 1472−1482

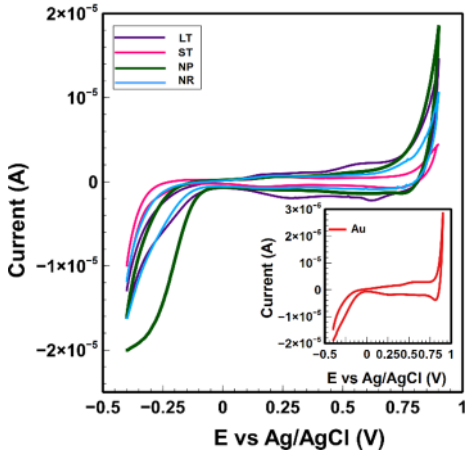

Figure 6. Cyclic voltammograms for potential windows measurement of various ZnO nanostructures and bare gold electrode (inset).

background current slightly increased, no considerable decrease of potential was observed for different ZnO morphologies; the potential window was around 1.2 V for all ZnO nanostructure types. The potential window was determined by the threshold current of 0.2−0.3 μA.

3.2.2. Electrochemical Reactions of Ferricyanide on the ZnO Electrode. It is known that the inner-sphere surface-sensitive ferricyanide ($[Fe(CN)_6]^{3-}$) redox couple is dependent on the electrochemical reactivity and surface morphology of the working electrode. For example, in the reversible system the electrochemical peak separation (ΔE_p) can be used to determine the number of electrons transferred; accordingly, a fast one-electron process exhibits ΔE_p = 59 mV.[65,66]

As a result, to investigate electronic carrier transport in various ZnO nanostructures, the reversible redox couple of ferricyanide/ferrocyanide was used. The cyclic voltammetry of the redox reaction including $[Fe(CN)_6]^{3-/4-}$ (100 μM) in a 0.1 M KCl solution (Figure 7) was employed to evaluate the potential window of ZnO electrodes.

The electron transfer rate is faster than the rate of ferricyanide diffusion from the solution to the electrode surface due to the concentration gradient, which forms due to ferricyanide reduction to ferrocyanide. The theoretical value of one-electron transfer in the ideal case would be ΔE_{pT} = 0.059 V at 298 K.[66] Therefore, the peak current I_p (measured as the distance from the baseline to the peak) is dependent on the active area of the electrode as is calculated by using the Randles−Sevcik equation,[67,68] where the constant $k_2 = 2.2 \times 10^5$ and D is the diffusion coefficient, $D = 7.2 \times 10^{-6}$ cm^2 s^{-1} for $[Fe(CN)_6]^{3-/4-}$.[69,70]

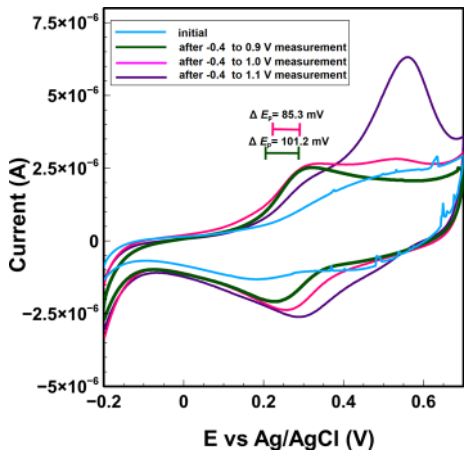

Figure 7. Cyclic voltammograms of $[Fe(CN)_6]^{3-/4-}$ for LT via changing potential window interval.

It can be noted that anodic and cathodic peaks have a symmetric shape for ST, LT, and NR curves which indicates the reversible redox reaction of ferricyanide occurred in these systems. However, the electrode covered with NPs has an asymmetric shape which indicates an irreversible redox reaction, which can be associated with the lower surface area and pore size.

The dependence of the peak-to-peak separation ΔE_p on various factors such as temperature, sweep rate, active surface, various materials and their defects, electrolyte and its concentration, and pH value are mostly studied.[49−52,65,66] The electron transfer rate can be evaluated by using ΔE_p, which corresponds to the potential difference between the oxidation and reduction peaks in the cyclic voltammograms. To measure the oxidation peak, the potential window was changed by altering the voltage interval. By the increase of the voltage to 1.1 V the oxidation peak changes from 0.4 to 0.7 V (Figure 7). The spreading −0.4 to 1.0 V indicates Au dissolution.[71,72] To determine the accurate ΔE_p value, the −0.4 to 1.0 V interval for the potential window measuring was further used.

Figures 8a and 8b show cyclic voltammograms of $[Fe(CN)_6]^{3-/4-}$ for the different morphologies of ZnO nanomaterials and the bare Au electrode. The ΔE_p decreased from 230.7 mV (for NP) to 61.7 mV (for LT). This decrease indicates an enhancement in electrochemical activity because of the changing ZnO surface area and surface morphology (Figures 8c and 8d). Larger than 0.059 V, ΔE_p indicate that ferricyanide molecules were not adsorbed but were free to diffuse toward the electrode surface,[73] as it can be noticed in Figure 8a,c.

3.2.3. Mechanisms Influencing Electrochemical Performance of Various ZnO Nanomaterials. The electrochemical properties of ZnO nanostructures are influenced by two simultaneous mechanisms: (i) the electrochemical reactions of ZnO nanostructures under different potentials and (ii) the electrochemical reactions of ferricyanide on the ZnO electrode. The electrochemical reaction of ferricyanide using electrodes with various ZnO morphologies is considered as a diffusion-controlled process similar to the single electron transfer quasi-reversible electrochemical process.[73] The best results are reached by using the electrode covered with LT which has the biggest active surface (0.095 cm^2) and its practical ΔE_p value of 61.7 mV, which is close to the theoretical 59 mV (Figure 7d). Consequently, a higher active area is connected to a higher electron transfer rate. Low or close to the theoretical ΔE_p value indicates a kinetically favorable route which minimizes background current and hence indicates electrode suitability for possible applications, e.g., biosensing.[49,50,52]

The high aspect ratio of the tetrapods might also lead to a higher electron conduction through the layer. ZnO nanostructure resistivity measurements showed resistivity of STs and LTs in the order of 10^2 Ω·m (Figure 9), which is consistent with earlier results,[74] whereas other ZnO nanostructures demonstrated an order of magnitude higher resistivity. The low resistivity of ZnO tetrapods could be associated with the one-dimensional morphology of their legs, which could

https://dx.doi.org/10.1021/acs.jpcc.0c08459
J. Phys. Chem. C 2021, 125, 1472−1482

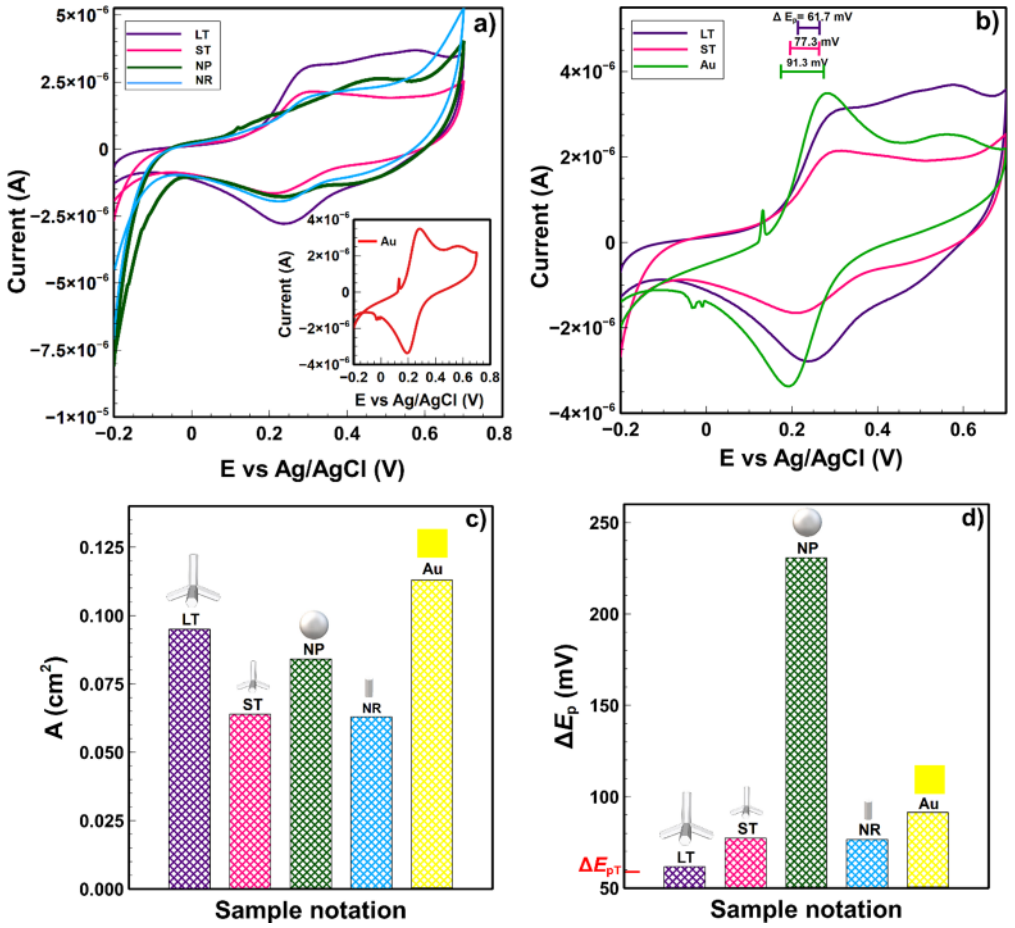

Figure 8. (a) Cyclic voltammograms of $[Fe(CN)_6]^{3-/4-}$ measured for electrodes, coated with ZnO nanostructures. (b) Cyclic voltammogram of $[Fe(CN)_6]^{3-/4-}$ measured for glass electrode covered with bare gold without ZnO materials. ΔE_p values are denoted by bars at the top. (c) Active area and (d) ΔE_p values for different ZnO morphology. The theoretical ΔE_{pT} = 59 mV value is marked on the axis.

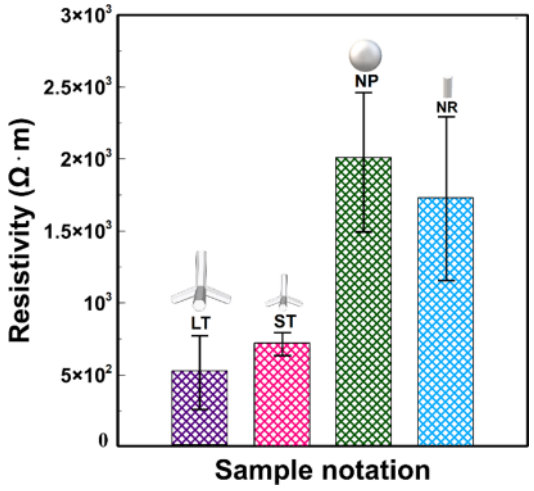

Figure 9. Resistivity measurement of ZnO nanostructures.

provide a direct and stable pathway for rapid electron transport.[75]

The electrochemical performance of ZnO nanomaterials may be affected by electron transfer at the surface active sites and by the conduction through the layer from the active site to the electrode. The quality of the crystal influences the electron transfer rate at the surface, since surface defects can act as active sites for electron transfer.[76] However, the direct electron conduction from the active sites to the electrode is important, as the resistance of the material can increase the peak separation due to voltage drop in the material.[77,78] Because ZnO nanostructures have the same crystal structure, their resistivity is mostly determined by the barriers at the particle–particle junctions, formed at the electron percolation path through the ZnO nanostructure layer from the surface to the Au electrode, as it is shown schematically in Figure 10. The specific ZnO tetrapod geometry of elongated legs spreading radially in four different directions gives the advantage of fewer barriers on the percolation path ensuring lower voltage drop, whereas a lower aspect ratio ZnO morphology (NP and NR)

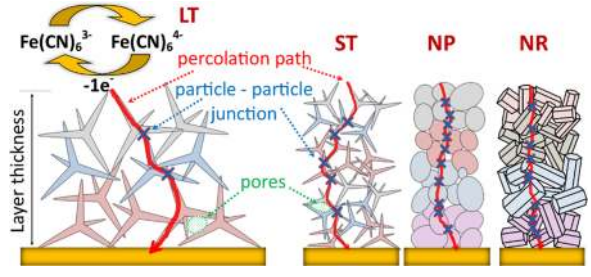

Figure 10. Electron transport in ZnO nanostructures: schematics of percolation path (red) through the ZnO nanostructure layer with the marked barriers (blue crosses) at the particle–particle junctions.

https://dx.doi.org/10.1021/acs.jpcc.0c08459
J. Phys. Chem. C 2021, 125, 1472–1482

percolation path encounters more junctions deteriorating the electron conduction, which is consistent with the resistivity measurements.

Different ZnO nanostructure morphology influences the layer packing during deposition, influencing pore sizes and forms. Consequently, reactant diffusion in ZnO nanostructures electrodes affects the electron transfer rate. ZnO tetrapods (LTs and STs) were characterized by the smallest pores, and it can be assumed that there is a lack of intercluster pores, which might indicate peculiar pores with openings only at one end at two ends (through pores), which could cause the $[Fe(CN)_6]^{3-/4-}$ molecule easier to adsorb and react on the surface.[62]

Consequently, the unique structure of tetrapods shows better electrochemical properties compared to other ZnO nanostructure counterparts due to geometry of their one-dimensional legs arranged in four directions, leading to more efficient electron transfer from the active site to the electrode; at the same time the ZnO tetrapod layer packing during deposition results in both high porosity and active area, ensuring low peak separation. The effect is more pronounced for longer leg tetrapods (LTs), leading to peak separation ΔE_p, approaching the theoretical value.

4. CONCLUSIONS

We examined the influence of the ZnO nanostructure morphology on the electrochemical properties using cyclic voltammetry and potential window measurements. Compared to ZnO nanorods and nanoparticles, ZnO tetrapods demonstrated better electrochemical properties. Interestingly, the larger tetrapods (LT diameter of 120 nm and ST diameter of 40 nm) showed the highest active surface value (0.095 cm^2) and a ΔE_p of 61.7 mV, which is close to the theoretical ZnO value (59 mV). UV−vis analysis showed a blue-shift in connection with the decrease of ZnO nanostructures size, which can be associated with the quantum size effect. Moreover, with the increase of the ZnO nanostructure size and shape, the slope of the shoulders became steeper since the scattering effects dominate. The one-dimensional legs arrangement of ZnO tetrapods compared to other ZnO nanostructure counterparts leads to superior electrochemical properties due to more efficient electron conduction; at the same time both porosity and active area are kept high as a result of prevented packing. The effect is more pronounced for longer leg tetrapods (LTs), leading to peak separation ΔE_p, approaching the theoretical value. These results are important for the future ZnO nanostructure applications in electrochemistry, where the influence of morphology on the properties should be considered.

AUTHOR INFORMATION

Corresponding Author

Simas Rackauskas − *Faculty of Mathematics and Natural Sciences and Institute of Materials Science, Kaunas University of Technology, Kaunas 50254, Lithuania;* orcid.org/0000-0002-8964-5299; Email: simas.rackauskas@ktu.lt

Authors

Agne Sulciute − *Faculty of Mathematics and Natural Sciences, Kaunas University of Technology, Kaunas 50254, Lithuania*

Keita Nishimura − *Institute of Materials and Systems for Sustainability, Nagoya University, Aichi 4648603, Japan*

Evgeniia Gilshtein − *Empa, Swiss Federal Laboratories for Materials Science and Technology, Dübendorf 8600, Switzerland;* orcid.org/0000-0001-5938-2523

Federico Cesano − *Department of Chemistry and NIS Interdepartmental Center and INSTM Reference Centre, University of Torino, Torino 10125, Italy*

Guido Viscardi − *Department of Chemistry and NIS Interdepartmental Center and INSTM Reference Centre, University of Torino, Torino 10125, Italy*

Albert G. Nasibulin − *Laboratory of Nanomaterials, Skolkovo Institute of Science and Technology, Moscow 143025, Russia; Department of Chemistry and Materials Science, Aalto University School of Chemical Engineering, Espoo 02015, Finland;* orcid.org/0000-0002-1684-3948

Yutaka Ohno − *Institute of Materials and Systems for Sustainability, Nagoya University, Aichi 4648603, Japan*

Complete contact information is available at: https://pubs.acs.org/10.1021/acs.jpcc.0c08459

Author Contributions

The manuscript was written through contributions of all authors. All authors have given approval to the final version of the manuscript. Conceptualization and methodology: A.S., Y.O., and S.R.; formal analysis: A.S., N.K., F.C., E.G., and S.R.; investigation: A.S., N.K., and S.R.; data curation: A.S.; writing—original draft preparation: A.S. and S.R.; writing—review and editing: A.S., G.V., A.N., Y.O., and S.R.; visualization: A.S. and S.R.; supervision and funding acquisition: S.R. All authors have read and agreed to the published version of the manuscript.

Notes

The authors declare no competing financial interest.

ACKNOWLEDGMENTS

This research was funded by the European Regional Development Fund, "Targeted research in the area of smart specialization" measure, Project 01.2.2-LMT-K-718-02-0011.

ABBREVIATIONS

BET, Brunauer−Emmett−Teller; CE, counter electrode; DFT, density functional theory; FWHM, full width at half-maximum; ICDD, International Centre for Diffraction Data; ITO, indium tin oxide; LT, large tetrapod; NP, nanoparticle; NR, nanorod; PSD, the associated pore size distribution; SEM, scanning electron microscopy; ST, small tetrapod; TEM, transmission electron microscopy; UV−vis, UV−vis spectroscopy; XRD, X-ray powder diffraction; ZnO-Ts, ZnO tetrapods.

REFERENCES

(1) Larina, O. V.; Kyriienko, P. I.; Balakin, D. Y.; Vorokhta, M.; Khalakhan, I.; Nychiporuk, Y. M.; Matolín, V.; Soloviev, S. O.; Orlyk, S. M. Effect of ZnO on Acid-Base Properties and Catalytic Performances of ZnO/ZrO2-SiO_2 Catalysts in 1,3-Butadiene Production from Ethanol-Water Mixture. *Catal. Sci. Technol.* **2019**, *9* (15), 3964−3978.

(2) Jiang, Z.; Soltanian, S.; Gholamkhass, B.; Aljaafari, A.; Servati, P. Light-Soaking Free Organic Photovoltaic Devices with Sol-Gel Deposited ZnO and AZO Electron Transport Layers. *RSC Adv.* **2018**, *8* (64), 36542−36548.

(3) Han, J.; Fan, F.; Xu, C.; Lin, S.; Wei, M.; Duan, X.; Wang, Z. L. ZnO Nanotube-Based Dye-Sensitized Solar Cell and Its Application in Self-Powered Devices. *Nanotechnology* **2010**, *21* (40), 405203.

(4) Mirzaei, A.; Kim, H. W.; Kim, S. S.; Neri, G. Nanostructured Semiconducting Metal Oxide Gas Sensors for Acetaldehyde Detection. *Chemosensors* **2019**, *7* (4), 56.
(5) Phan, D. T.; Chung, G. S. Surface Acoustic Wave Hydrogen Sensors Based on ZnO Nanoparticles Incorporated with a Pt Catalyst. *Sens. Actuators, B* **2012**, *161* (1), 341−348.
(6) Bhati, V. S.; Hojamberdiev, M.; Kumar, M. Enhanced Sensing Performance of ZnO Nanostructures-Based Gas Sensors: A Review. *Energy Reports* **2020**, *6*, 46−62.
(7) Liu, X.; Chen, N.; Xing, X.; Li, Y.; Xiao, X.; Wang, Y.; Djerdj, I. A High-Performance *n*-Butanol Gas Sensor Based on ZnO Nanoparticles Synthesized by a Low-Temperature Solvothermal Route. *RSC Adv.* **2015**, *5* (67), 54372−54378.
(8) Chaudhary, S.; Umar, A.; Bhasin, K. K.; Baskoutas, S. Chemical Sensing Applications of ZnO Nanomaterials. *Materials* **2018**, *11* (2), 287.
(9) Leonardi, S. Two-Dimensional Zinc Oxide Nanostructures for Gas Sensor Applications. *Chemosensors* **2017**, *5* (2), 17.
(10) Shi, Y.; Bao, S.; Shi, R.; Huang, C.; Amini, A.; Wu, Z.; Zhang, L.; Wang, N.; Cheng, C. Y-Shaped ZnO Nanobelts Driven from Twinned Dislocations. *Sci. Rep.* **2016**, DOI: 10.1038/srep22494.
(11) Moezzi, A.; McDonagh, A. M.; Cortie, M. B. Zinc Oxide Particles: Synthesis, Properties and Applications. *Chem. Eng. J.* **2012**, *185-186*, 1−22.
(12) Kantharia, M.; Mishra, P.; Trivedi, M. K. Strength of Cement Mortar Using Nano Oxides: An Experimental Study. *Int. J. Eng. Adv. Technol.* **2019**, *8* (3), 294−299.
(13) Nochaiya, T.; Sekine, Y.; Choopun, S.; Chaipanich, A. Microstructure, Characterizations, Functionality and Compressive Strength of Cement-Based Materials Using Zinc Oxide Nanoparticles as an Additive. *J. Alloys Compd.* **2015**, *630*, 1−10.
(14) Polsongkram, D.; Chamninok, P.; Pukird, S.; Chow, L.; Lupan, O.; Chai, G.; Khallaf, H.; Park, S.; Schulte, A. Effect of Synthesis Conditions on the Growth of ZnO Nanorods via Hydrothermal Method. *Phys. B* **2008**, *403* (19−20), 3713−3717.
(15) Escobedo Morales, A.; Herrera Zaldivar, M.; Pal, U. Indium Doping in Nanostructured ZnO through Low-Temperature Hydrothermal Process. *Opt. Mater. (Amsterdam, Neth.)* **2006**, *29* (1), 100−104.
(16) Scarano, D.; Cesano, F.; Bertarione, S.; Zecchina, A. Zinc Oxide Nanostructures: From Chestnut Husk-like Structures to Hollow Nanocages, Synthesis and Structure. *Crystals* **2018**, *8* (4), 153.
(17) Rackauskas, S.; Mustonen, K.; Järvinen, T.; Mattila, M.; Klimova, O.; Jiang, H.; Tolochko, O.; Lipsanen, H.; Kauppinen, E. I.; Nasibulin, A. G. Synthesis of ZnO Tetrapods for Flexible and Transparent UV Sensors. *Nanotechnology* **2012**, *23* (9), 095502.
(18) Rackauskas, S.; Klimova, O.; Jiang, H.; Nikitenko, A.; Chernenko, K. A.; Shandakov, S. D.; Kauppinen, E. I.; Tolochko, O. V.; Nasibulin, A. G. A Novel Method for Continuous Synthesis of ZnO Tetrapods. *J. Phys. Chem. C* **2015**, *119* (28), 16366−16373.
(19) Mishra, Y. K.; Adelung, R. ZnO Tetrapod Materials for Functional Applications. *Mater. Today* **2018**, *21*, 631−651.
(20) Scarano, D.; Bertarione, S.; Cesano, F.; Vitillo, J. G.; Zecchina, A. Plate-like Zinc Oxide Microcrystals: Synthesis and Characterization of a Material Active toward Hydrogen Adsorption. *Catal. Today* **2006**, *116* (3), 433−438.
(21) Šulčiute, A.; Valatka, E. Electrodeposition and Photoelectrocatalytic Activity of ZnO Films on AISI 304 Type Steel. *Medziagotyra* **2012**, *18* (4), 318−324.
(22) Liu, Y.; Gorla, C. R.; Liang, S.; Emanetoglu, N.; Lu, Y.; Shen, H.; Wraback, M. Ultraviolet Detectors Based on Epitaxial ZnO Films Grown by MOCVD. *J. Electron. Mater.* **2000**, *29* (1), 69−74.
(23) Kaiya, K.; Omichi, K.; Takahashi, N.; Nakamura, T.; Okamoto, S.; Yamamoto, H. Epitaxial Growth of ZnO Thin Films Exhibiting Room-Temperature Ultraviolet Emission by Atmospheric Pressure Chemical Vapor Deposition. *Thin Solid Films* **2002**, *409*, 116−119.
(24) Kashiwaba, Y.; Haga, K.; Watanabe, H.; Zhang, B. P.; Segawa, Y.; Wakatsuki, K. Structures and Photoluminescence Properties of ZnO Films Epitaxially Grown by Atmospheric Pressure MOCVD. *Phys. Status Solidi B* **2002**, *229* (2), 921−924.
(25) Cho, J.; Hwang, S.; Ko, D. H.; Chung, S. Transparent ZnO Thin-Film Deposition by Spray Pyrolysis for High-Performance Metal-Oxide Field-Effect Transistors. *Materials* **2019**, *12* (20), 3423.
(26) Ashkarran, A. A.; Iraji zad, A.; Mahdavi, S. M.; Ahadian, M. M. ZnO Nanoparticles Prepared by Electrical Arc Discharge Method in Water. *Mater. Chem. Phys.* **2009**, *118* (1), 6−8.
(27) Ashkarran, A. A.; Iraji Zad, A.; Mahdavi, S. M.; Ahadian, M. M. Photocatalytic Activity of ZnO Nanoparticles Prepared via Submerged Arc Discharge Method. *Appl. Phys. A: Mater. Sci. Process.* **2010**, *100* (4), 1097−1102.
(28) Kim, K. K.; Song, J. H.; Jung, H. J.; Choi, W. K.; Park, S. J.; Song, J. H. The Grain Size Effects on the Photoluminescence of ZnO/α-Al2O3 grown by Radio-Frequency Magnetron Sputtering. *J. Appl. Phys.* **2000**, *87* (7), 3573−3575.
(29) Nakahara, K.; Takasu, H.; Fons, P.; Iwata, K.; Yamada, A.; Matsubara, K.; Hunger, R.; Niki, S. Growth and Characterization of Undoped ZnO Films for Single Crystal Based Device Use by Radical Source Molecular Beam Epitaxy (RS-MBE). *J. Cryst. Growth* **2001**, *227−228*, 923−928.
(30) Villanueva, Y. Y.; Liu, D. R.; Cheng, P. T. Pulsed Laser Deposition of Zinc Oxide. *Thin Solid Films* **2006**, *501*, 366−369.
(31) Thu, T. V.; Maenosono, S. Synthesis of High-Quality Al-Doped ZnO Nanoink. *J. Appl. Phys.* **2010**, *107* (1), 014308.
(32) Bauermann, L. P.; Bill, J.; Aldinger, F. Bio-Friendly Synthesis of ZnO Nanoparticles in Aqueous Solution at near-Neutral PH and Low Temperature. *J. Phys. Chem. B* **2006**, *110* (11), 5182−5185.
(33) Sirelkhatim, A.; Mahmud, S.; Seeni, A.; Kaus, N. H. M.; Ann, L. C.; Bakhori, S. K. M.; Hasan, H.; Mohamad, D. Review on Zinc Oxide Nanoparticles: Antibacterial Activity and Toxicity Mechanism. *Nano-Micro Lett.* **2015**, *7* (3), 219−242.
(34) Yi, G. C.; Wang, C.; Park, W. Il. ZnO Nanorods: Synthesis, Characterization and Applications. *Semicond. Sci. Technol.* **2005**, *20*, S22.
(35) Ridhuan, N. S.; Abdul Razak, K.; Lockman, Z.; Abdul Aziz, A. Structural and Morphology of ZnO Nanorods Synthesized Using ZnO Seeded Growth Hydrothermal Method and Its Properties as UV Sensing. *PLoS One* **2012**, *7* (11), e50405.
(36) Abdelmohsen, A. H.; Rouby, W. M. A. E.; Ismail, N.; Farghali, A. A. Morphology Transition Engineering of ZnO Nanorods to Nanoplatelets Grafted Mo8O23-MoO2 by Polyoxometalates: Mechanism and Possible Applicability to Other Oxides. *Sci. Rep.* **2017**, DOI: 10.1038/s41598-017-05750-x.
(37) Demille, T. B.; Hughes, R. A.; Preston, A. S.; Adelung, R.; Mishra, Y. K.; Neretina, S. Light-Mediated Growth of Noble Metal Nanostructures (Au, Ag, Cu, Pt, Pd, Ru, Ir, Rh) From Micro- and Nanoscale ZnO Tetrapodal Backbones. *Front. Chem.* **2018**, *6*, 1−8.
(38) Shen, L.; Zhang, H.; Guo, S. Control on the Morphologies of Tetrapod ZnO Nanocrystals. *Mater. Chem. Phys.* **2009**, *114* (2−3), 580−583.
(39) Tawale, J. S.; Dey, K. K.; Pasricha, R.; Sood, K. N.; Srivastava, A. K. Synthesis and Characterization of ZnO Tetrapods for Optical and Antibacterial Applications. *Thin Solid Films* **2010**, *519*, 1244−1247.
(40) Mishra, Y. K.; Modi, G.; Cretu, V.; Postica, V.; Lupan, O.; Reimer, T.; Paulowicz, I.; Hrkac, V.; Benecke, W.; Kienle, L.; Adelung, R. Direct Growth of Freestanding ZnO Tetrapod Networks for Multifunctional Applications in Photocatalysis, UV Photodetection, and Gas Sensing. *ACS Appl. Mater. Interfaces* **2015**, *7* (26), 14303−14316.
(41) Goharshadi, E. K.; Ding, Y.; Jorabchi, M. N.; Nancarrow, P. Ultrasound-Assisted Green Synthesis of Nanocrystalline ZnO in the Ionic Liquid [Hmim][NTf2]. *Ultrason. Sonochem.* **2009**, *16* (1), 120−123.
(42) Khoshhesab, Z. M.; Sarfaraz, M.; Houshyar, Z. Influences of Urea on Preparation of Zinc Oxide Nanostructures Through Chemical Precipitation in Ammonium Hydrogencarbonate Solution.

Synth. React. Inorg., Met.-Org., Nano-Met. Chem. **2012**, *42* (10), 1363−1368.
(43) Verbič, A.; Gorjanc, M.; Simončič, B. Zinc Oxide for Functional Textile Coatings: Recent Advances. *Coatings* **2019**, *9* (9), 17−23.
(44) Kim, K.-B.; Kim, Y. W.; Lim, S. K.; Roh, T. H.; Bang, D. Y.; Choi, S. M.; Lim, D. S.; Kim, Y. J.; Baek, S.-H.; Kim, M.-K.; Seo, H.-S.; Kim, M.-H.; Kim, H. S.; Lee, J. Y.; Kacew, S.; Lee, B.-M. Risk Assessment of Zinc Oxide, a Cosmetic Ingredient Used as a UV Filter of Sunscreens. *J. Toxicol. Environ. Health, Part B* **2017**, *20* (3), 155−182.
(45) Sharma, J.; Vashishtha, M.; Shah, D. O. Crystallite Size Dependence on Structural Parameters and Photocatalytic Activity of Microemulsion Mediated Synthesized Zno Nanoparticles Annealed at Different Temperatures. *Glob. J. Sci. Front. Res. B Chem.* **2014**, *14* (5), 19−31.
(46) Li, Y.; Xia, Y.; Liu, K.; Ye, K.; Wang, Q.; Zhang, S.; Huang, Y.; Liu, H. Constructing Fe-MOF-Derived Z-Scheme Photocatalysts with Enhanced Charge Transport: Nanointerface and Carbon Sheath Synergistic Effect. *ACS Appl. Mater. Interfaces* **2020**, *12* (22), 25494−25502.
(47) Huang, Y.; Xu, H.; Yang, H.; Lin, Y.; Liu, H.; Tong, Y. Efficient Charges Separation Using Advanced BiOI-Based Hollow Spheres Decorated with Palladium and Manganese Dioxide Nanoparticles. *ACS Sustainable Chem. Eng.* **2018**, *6* (2), 2751−2757.
(48) Li, Y.; Liu, K.; Zhang, J.; Yang, J.; Huang, Y.; Tong, Y. Engineering the Band-Edge of Fe 2 O 3 /ZnO Nanoplates via Separate Dual Cation Incorporation for Efficient Photocatalytic Performance. *Ind. Eng. Chem. Res.* **2020**, *59* (42), 18865−18872.
(49) Lyons, M. E. G.; Keeley, G. P. The Redox Behaviour of Randomly Dispersed Single Walled Carbon Nanotubes Both in the Absence and in the Presence of Adsorbed Glucose Oxidase. *Sensors* **2006**, *6* (12), 1791−1826.
(50) Kim, M. Y.; Naveen, M. H.; Gurudatt, N. G.; Shim, Y. B. Detection of Nitric Oxide from Living Cells Using Polymeric Zinc Organic Framework-Derived Zinc Oxide Composite with Conducting Polymer. *Small* **2017**, *13* (26), 1700502.
(51) Wu, Q.; Hou, Y.; Zhang, M.; Hou, X.; Xu, L.; Wang, N.; Wang, J.; Huang, W. Amperometric Cholesterol Biosensor Based on Zinc Oxide Films on a Silver Nanowire-Graphene Oxide Modified Electrode. *Anal. Methods* **2016**, *8* (8), 1806−1812.
(52) Lim, A.; Zheng, T.; Andou, Y.; Zawawi, R. M. Effects of Deposition Parameters on the Electrochemical Behaviour of ZnO Thin Film. *Adv. Chem. Sci.* **2017**, *3* (4), 521−524.
(53) Bolis, V.; Fubini, B.; Giamello, E.; Reller, A. Effect of Form of the Surface Reactivity of Differently Prepared Zinc Oxides. *J. Chem. Soc., Faraday Trans. 1* **1989**, *85* (4), 855−867.
(54) Liu, Y.; Zhang, Z. Y.; Hu, Y. F.; Jin, C. H.; Peng, L. M. Quantitative Fitting of Nonlinear Current-Voltage Curves and Parameter Retrieval of Semiconducting Nanowire, Nanotube and Nanoribbon Devices. *J. Nanosci. Nanotechnol.* **2008**, *8* (1), 252−258.
(55) Thandavan, T. M. K.; Gani, S. M. A.; Wong, C. S.; Nor, R. M. Evaluation of Williamson−Hall Strain and Stress Distribution in ZnO Nanowires Prepared Using Aliphatic Alcohol. *J. Nondestruct. Eval.* **2015**, *34* (2), 1−9.
(56) Scarano, D.; Spoto, G.; Bordiga, S.; Zecchina, A.; Lamberti, C. Lateral Interactions in CO Adlayers on Prismatic ZnO Faces: A FTIR and HRTEM Study. *Surf. Sci.* **1992**, *276* (1−3), 281−298.
(57) Kroll, C.; Abraham, M.; Göpel, W. Step Structure Evolution on Electrostatic Neutral Zinc Oxide Vicinal Surfaces - Studied by Spot Profile Analysis - LEED. *Surf. Sci.* **1991**, *253* (1−3), 157−166.
(58) Zak, A. K.; Abrishami, M. E.; Majid, W. H. A.; Yousefi, R.; Hosseini, S. M. Effects of Annealing Temperature on Some Structural and Optical Properties of ZnO Nanoparticles Prepared by a Modified Sol−Gel Combustion Method. *Ceram. Int.* **2011**, *37* (1), 393−398.
(59) Zak, A. K.; Razali, R.; Majid, W. H. A.; Darroudi, M. Synthesis and Characterization of a Narrow Size Distribution of Zinc Oxide Nanoparticles. *Int. J. Nanomed.* **2011**, *6*, 1399−1403.
(60) Segets, D.; Gradl, J.; Taylor, R. K.; Vassilev, V.; Peukert, W. Analysis of Optical Absorbance Spectra for the Determination of ZnO Nanoparticle Size Distribution, Solubility, and Surface Energy. *ACS Nano* **2009**, *3* (7), 1703−1710.
(61) Cesano, F.; Bertarione, S.; Uddin, M. J.; Agostini, G.; Scarano, D.; Zecchina, A. Designing TiO_2 Based Nanostructures by Control of Surface Morphology of Pure and Silver Loaded Titanate Nanotubes. *J. Phys. Chem. C* **2010**, *114* (1), 169−178.
(62) Zdravkov, B. D.; Čermák, J. J.; Šefara, M.; Janků, J. Pore Classification in the Characterization of Porous Materials: A Perspective. *Cent. Eur. J. Chem.* **2007**, *5* (2), 385−395.
(63) Cullity, B. D.; Stock, S. R. *Elements of X-Ray Diffraction*, 3rd ed.; Prentice Hall: 2001; Chapter 1.
(64) Yokoyama, Y.; Fukutsuka, T.; Miyazaki, K.; Abe, T. Origin of the Electrochemical Stability of Aqueous Concentrated Electrolyte Solutions. *J. Electrochem. Soc.* **2018**, *165* (14), A3299−A3303.
(65) Wang, J. *Analytical Electrochemistry, Third Edition* **2006**, DOI: 10.1002/0471790303.
(66) Eisele, S.; Schwarz, M.; Speiser, B.; Tittel, C. Diffusion Coefficient of Ferrocene in 1-Butyl-3-Methylimidazolium Tetrafluoroborate - Concentration Dependence and Solvent Purity. *Electrochim. Acta* **2006**, *51* (25), 5304−5306.
(67) Shetti, N. P.; Nayak, D. S.; Malode, S. J.; Kulkarni, R. M. Electrochemical Sensor Based upon Ruthenium Doped TiO_2 Nanoparticles for the Determination of Flufenamic Acid. *J. Electrochem. Soc.* **2017**, *164* (5), B3036−B3042.
(68) García-Miranda Ferrari, A.; Foster, C. W.; Kelly, P. J.; Brownson, D. A. C.; Banks, C. E. Determination of the Electrochemical Area of Screen-Printed Electrochemical Sensing Platforms. *Biosensors* **2018**, *8* (2), 53.
(69) Konopka, S. J.; McDuffie, B. Diffusion Coefficients of Ferri- and Ferrocyanide Ions in Aqueous Media, Using Twin-Electrode Thin-Layer Electrochemistry. *Anal. Chem.* **1970**, *42* (14), 1741−1746.
(70) Pumera, M.; Sasaki, T.; Iwai, H. Relationship between Carbon Nanotube Structure and Electrochemical Behavior: Heterogeneous Electron Transfer at Electrochemically Activated Carbon Nanotubes. *Chem. - Asian J.* **2008**, *3* (12), 2046−2055.
(71) Ren, B.; Picardi, G.; Pettinger, B. Preparation of Gold Tips Suitable for Tip-Enhanced Raman Spectroscopy and Light Emission by Electrochemical Etching. *Rev. Sci. Instrum.* **2004**, *75* (4), 837−841.
(72) Narasiwodeyar, S.; Dwyer, M.; Liu, M.; Park, W. K.; Greene, L. H. Two-Step Fabrication Technique of Gold Tips for Use in Point-Contact Spectroscopy. *Rev. Sci. Instrum.* **2015**, *86* (3), 033903.
(73) Feng, G.; Xiong, Y.; Wang, H.; Yang, Y. Cyclic Voltammetry Investigation of Diffusion of Ferrocene within Propylene Carbonate Organogel Formed by Gelator. *Electrochim. Acta* **2008**, *53* (28), 8253−8257.
(74) Oku, M. Electrical Conductivity of Tetrapod-Shaped Zno Whiskers. *Jpn. J. Appl. Phys.* **1993**, *32* (9), 4377−4379.
(75) Wei, N.; Cui, H.; Wang, X.; Xie, X.; Wang, M.; Zhang, L.; Tian, J. Hierarchical Assembly of In2O3 Nanoparticles on ZnO Hollow Nanotubes Using Carbon Fibers as Templates: Enhanced Photocatalytic and Gas-Sensing Properties. *J. Colloid Interface Sci.* **2017**, *498*, 263−270.
(76) Zhou, W. Y.; Liu, J. Y.; Song, J. Y.; Li, J. J.; Liu, J. H.; Huang, X. J. Surface-Electronic-State-Modulated, Single-Crystalline (001) TiO_2 Nanosheets for Sensitive Electrochemical Sensing of Heavy-Metal Ions. *Anal. Chem.* **2017**, *89* (6), 3386−3394.
(77) Wang, J. X.; Sun, X. W.; Wei, A.; Lei, Y.; Cai, X. P.; Li, C. M.; Dong, Z. L. Zinc Oxide Nanocomb Biosensor for Glucose Detection. *Appl. Phys. Lett.* **2006**, *88* (23), 233106.
(78) Liu, J.; Guo, C.; Li, C. M.; Li, Y.; Chi, Q.; Huang, X.; Liao, L.; Yu, T. Carbon-Decorated ZnO Nanowire Array: A Novel Platform for Direct Electrochemistry of Enzymes and Biosensing Applications. *Electrochem. Commun.* **2009**, *11* (1), 202−205.

https://dx.doi.org/10.1021/acs.jpcc.0c08459
J. Phys. Chem. C 2021, 125, 1472−1482